Conference on Modelling Fluid Flow (CMFF'22)
The 18th International Conference on Fluid Flow Technologies
Budapest, Hungary, August 30 -September 2, 2022

INITIATION OF BIFURCATION ANEURYSMS: A PILOT STUDY

Péter FRIEDRICH[1], Benjamin CSIPPA[2], György PAÁL[3], István SZIKORA

[1] Corresponding Author. Department of Hydrodynamic Systems, Faculty of Mechanical Engineering, Budapest University of Technology and Economics. Műegyetem rkp 3., H-1111 Budapest, Hungary. Tel.: +36 1 463 1680, E-mail: Friedrich.peti@gmail.com
[2] Department of Hydrodynamic Systems, Faculty of Mechanical Engineering, Budapest University of Technology and Economics. E-mail: bcsippa@hds.bme.hu
[3] Department of Hydrodynamic Systems, Faculty of Mechanical Engineering, Budapest University of Technology and Economics. E-mail: gypaal@hds.bme.hu
4 Department of Neurointerventions, National Institute of Mental Health, Neurology and Neurosurgery. E-mail: h13424szi@ella.hu

ABSTRACT

Intracranial aneurysms are saccular lesions forming on the vessel wall of brain arteries. The most common type is the bifurcation aneurysm located at the sites of arterial junctions. The exact cause of the disease is not yet understood as it involves a complex cascade of physical and biochemical processes. According to the current hypothesis the hemodynamic fluid forces due to wall-shear stresses initiate a biochemical process in the innermost layer of the vessel, the endothelium. In this study our objective was to analyse the flow field near the vessel wall before the aneurysm inception. Five bifurcation aneurysms and five control cases were selected for numerical comparison. The aneurysms were removed virtually by an objective interpolation method to reconstruct the vessel shape before the emergence of the aneurysm. For each geometry a time-varying inlet velocity-profile with outlet flow rates according to Murray's law were set case-specifically. Velocity vectors were decomposed to axial and secondary - radial and circumferential - components and evaluated throughout a centreline originating from one outlet to the accompanying outlet of the bifurcation. Inherently, secondary flow features emerge at a vessel bifurcation in all cases. However, in the cases of aneurysmal geometries, elevated secondary flow activities were found.

Keywords: Aneurysm, Bifurcation, CFD, Digital reconstruction, IA-initiation, Murray's law

NOMENCLATURE

$\underline{Fr}$	[-]	frenet unit vector
$\underline{r}$	[-]	vector
p	[-]	arbitrary point in plane
r_c	[-]	centreline point in plane
$\underline{v}$	[m/s]	absolute velocity vector

Subscripts and Superscripts

n, b, t	normal, binormal, tangent components of the Frenet system
ax	axial velocity
sec	secondary velocity
rad	radial component
circ	circumferential velocity
x, y, z	axes
$-$	temporal mean

1. INTRODUCTION

Aneurysms are a dangerous medical condition on the arteries of the human body. They come in two distinct shapes. The first one is barrel like called fusiform and usually form on the aorta, the other ones are the saccular berry-shaped aneurysms. They mostly manifest themselves on arteries inside the brain, either on the side of an artery or at a junction of arteries, called bifurcations as it can be seen on Figure 1 in pink. Regardless of the form of the aneurysm their danger lies in the fact that they do not carry specific symptoms and can be lethal. The most common way for an aneurysm to cause problem is a rapture. A rupture can occur due to weakened walls Ruptures can also be caused by external factors such as getting the head hit. Risk of aneurysm formation increases with age, but high blood pressure and genetics also play a role. [1]

Modern medical techniques allow the treatment of aneurysm with minimally invasive methods. The affected area is reached through the arteries by a micro catheter. A flow diverter stent is placed at the opening of the aneurysm to stabilize the vessel wall and to restrict blood flow in to the aneurysm sack, causing the blood inside the sack to coagulate.

The exact cause and pathophysiology of the disease is not yet understood as it involves complex physical and biomechanical processes. According to the current hypothesis in hemodynamics the Wall

Shear Stress (WSS) caused by fluid forces on the inner layer of the vessel, the endothelium, initiate a biomechanical process resulting in the formation of an aneurysm. It is accepted that the wall shear stress field is highly sensitive to the small alterations of the surface of the 3D model. This model is made by a non-medical professional in a subjective way, thus resulting in a less robust surface. WSS is also dependent on the way of smoothing of the surface. It is accepted that the velocity field is more robust and is less dependent on small surface alternations than WSS [2][3].

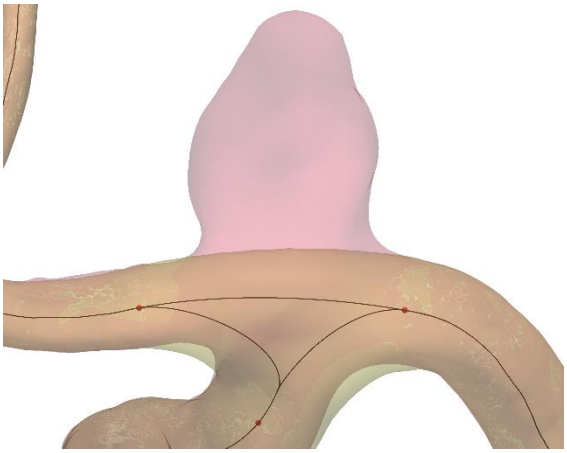

Figure 1. Bifurcation aneurysm, interpolated centrelines can be seen in black, the clipping points in red, and the reconstructed model in yellow. This is a worst-case scenario; the thickening of the bifurcation section is a rare occurrence.

In this paper the secondary velocity field is studied on 4 geometries with bifurcation aneurysms in the pre-disease state using digital reconstruction. There are also 4 control cases without aneurysms to compare the velocity fields at the bifurcation.

2. METHOD

2.1 Digital Reconstruction

Three cases out of the total 8 were provided in the form of DSA images under the National Brain Research Program of Hungary. The rest were obtained as surface models from the Aneurysk [4] database. The DSA images were captured with a GE Innova device, with the resolution of 0.22 mm.

DSA imaging is a medical imaging method using a contrast agent to show the arteries on the image. The above-mentioned cases were segmented using the program called Slicer 4.10.2, which uses a marching cubes algorithm to compute the surface, and applies a smoothing to the surface, as the algorithm generates a rough surface.

Subsequently, follows the digital reconstruction to remove the aneurysm and restoration of the parent vessel to the pre-disease state. The procedure was performed with the algorithms of Morphman [5][6], an open-source program based on the Vascular Modelling Tool Kit. The removal can be done using the bifurcation manipulation component. It was designed for the changing of angles between the outflow arteries, but by setting the angle change to zero degrees it can be used to remove a bifurcation aneurysm. The algorithm follows the same steps as those previously used in VMTK. First, computation of the centrelines and the Voronoi diagram of the model is performed. The diagram contains the radius of the maximum inscribed sphere to every point of the centreline. It is used to represent the surface around the centreline. In the next step the domain of interest is defined, either by coordinates or by using a 3D view of the model and selecting two relevant outlets of the bifurcation. Using this data, an algorithm finds the diverging points of the centrelines at the bifurcation region and cuts all 5 of the centrelines. One is going between the outlets, two from the inlet to the outlets, and two from the outlets into the aneurysm. Further back from the diverging points also marks the planes where in-between the section of the Voronoi diagram will be removed [7]. These points are called clipping points. The next step involves the interpolation of the centrelines and the Voronoi diagram, both are done by objective interpolation algorithms. In this step Morphman differs from the VMTK method optionally. In VMTK, first the centrelines are interpolated from the inlet to the outflow sides, just these two. Then the Voronoi diagram gets interpolated from the three clipping points towards each other, but only between the inlet and the outlets, and not between the two outlets across the bifurcation. In Morphman by setting the “bifurcation” option to true, it also computes an interpolated centreline between the two outlets across the bifurcation and uses up this line when interpolating the Voronoi diagram. The clipping points and the interpolated centrelines can be seen in Fig. 1. The effects of this method will be shown in the next step, surface generation. Using the interpolated Voronoi diagram, the surface of the geometry can be computed by the inscribed sphere radii. If using VMTK the bifurcation will have a notch on top of the bifurcation, because only the centrelines going from the inlet to the outlets were used for the interpolation. With Morphman, enabling the above-mentioned option, the reconstructed surface does not have this notch, and is more representative of the pre disease state of the bifurcation [8]. The last step is smoothing the surface before output.

The reconstructed models underwent additional modifications to prepare them for simulation. First the inlet and outlet profiles were extended by 8 diameters and adapted to a circular shape. This is done to ensure properly developed flow through profiles at the investigated regions [3].

2.2 Simulation

The following section will cover the Computational Fluid Dynamic (CFD) simulation, from meshing, through boundary conditions to running settings. Everything related to the above was carried out using ANSYS components. For meshing Mesher was used, and the simulations were run in CFX.

The surfaces were open at the boundaries after the reconstruction and needed to be closed. This was done using Space Claim. The cross-sectional areas of the inlets and outlets were also measured in this step for computing the boundary conditions.

The numerical mesh for the simulations were done with the same parameters. The tetrahedron cells were chosen. Ten inflation layers were used adjacent to the vessel wall with a growth factor of 1.1. The target value for skewness was set to 0.8. These resulted in meshes with around 5 million elements in size.

Transient simulations were run, with adaptive timesteps and a Courant number of 0.8. Three heartbeat cycles were simulated, each 0.8 seconds long. Only the data of the third cycle were exported for post-processing to eliminate the effect of numerical transients. The arterial walls were assumed to be rigid, and blood to be a Newtonian fluid. The last assumption may cause error, but the error of not perfect rheology is much smaller compared to one caused by the subjectivity in the segmentation process. Table 1 contains all the simulation settings.

Patient-specific boundary conditions were set to each geometry. The inlet was a velocity inlet. The velocity was calculated according to scaling law that was experimentally obtained using the area of the inlet [9]. The calculated velocity was a cross-sectional average. The heart cycle waveform that can be seen in Figure 2 [10]. was imposed on the inlet with a parabolic velocity profile. The used heart cycle profile was 0.8 seconds long.

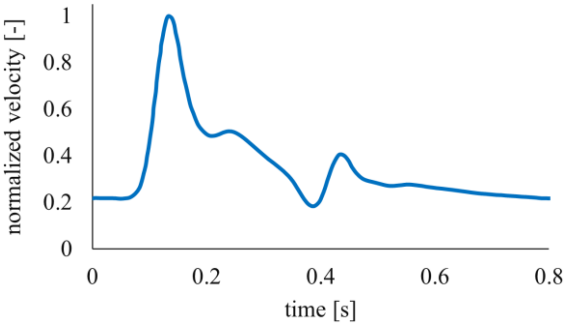

Figure 2. The normalized velocity waveform used as input for the heart-rate cycle.

Mass flow outlets were set as outlet boundary conditions according to Murray's law, except for the smallest one, which was an opening with 0Pa. Aneutools was used for computing the mass flow percentage on each outlet [11]. It was originally developed for the Internal Carotid Artery (ICA), but it was used even when the bifurcation was higher up than the ICA bifurcation, as there is no accepted method of setting boundary conditions for that section. This also means, that in these cases the whole ICA section was simulated as well.

Table 1. Parameters of the simulations

ID	Mean inlet velocity [m/s]	Reynolds-number [-]	Inlet area [mm^2]
C0035	0.2548	417.48	21.90
C0064	0.1770	233.36	14.19
C0066_c	0.1670	218.80	13.52
C0086	0.1858	252.28	15.04
C0066	0.1670	218.80	13.52
NAP191230C	0.2145	317.17	17.84
NAP200812C	0.2426	386.06	20.66
NAP200909C	0.2790	482.58	24.40

For post processing the results were exported in a format that can be used in ParaView.

2.3 Post-processing

The post-processing was done by in-house built Python scripts. In the centre of the post processing is the Frenet system, thus, having a clear understanding of these orthogonal coordinate systems is essential.

Each geometry has centrelines defined. In each point of the centreline an orthogonal coordinate system can be defined. In case of a Frenet system each of the three axes point in a specific direction. The Frenet tangent vector $\underline{Fr_t}$ is parallel to the tangent of the centreline at that point. The Frenet normal vector $\underline{Fr_n}$ is perpendicular to the Frenet tangent vector, and points towards the centre of the tangent circle of the centreline. The third axis is the Frenet binormal vector $\underline{Fr_b}$ and is perpendicular to the other two axes. All of them are unit vectors. The geometry can be sliced with a plane defined by the frenet normal and binormal vectors, creating a cross section of the artery perpendicular to the centreline. All further calculations were done in these slices along the centreline at each point.

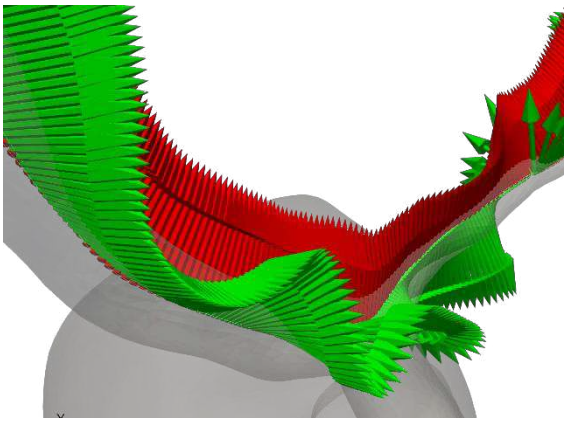

Figure 3. Effect of Frenet smoothing, green non smoothed, red smoothed

Centrelines for post-processing were calculated and smoothed with a distance of 0.15 mm between the points. An optimal smoothing factor and iterations must be used to compute a smooth, but true centreline, smoothing factor was set to 1.2 and the number of iterations to 100 [12]. Centreline smoothing helps smooth out the sudden orientation changes of the frenet systems, but it is not perfect. In this study for bifurcation aneurysms the slicing of the geometry went between the two outlets of the bifurcation. For the calculations, the Frenet systems needed to have slow orientation change along the length of the centreline. To achieve this a properly smoothed temporary centreline was computed, with the same number of points as the previous one, and then the Frenet systems were interpolated to the points of that centreline. This resulted in a Frenet system with the same orientation along the centreline as can be seen on Fig. 3.

Using the Frenet systems the velocity field in a slice can be decomposed to an axial and a secondary component. The axial component can be calculated using the Frenet tangent unit vector as seen in Eq. (1). Then by using Eq. (2) the secondary velocity vector is calculated by subtracting $\underline{v}_{ax}$ from the velocity vector $\underline{v}$.

$$\underline{v}_{ax} = (\underline{v} \cdot \underline{Fr}_t) \cdot \underline{Fr}_t \tag{1}$$

$$\underline{v}_{sec} = \underline{v} - \underline{v}_{ax} \tag{2}$$

The secondary flow can be further separated into radial and circumferential components by switching to a local polar coordinate system around the centreline point r_c in the slice. In order to decompose the secondary velocity to these components, first a radial unit vector was defined by Eq. (3) between the centreline and an arbitrary point p in the slice. Thus, the radial velocity $\underline{v}_{rad}$ can be calculated as seen in Eq. (4). The circumferential velocity $\underline{v}_{cir}$ is calculated by subtracting the radial component from the secondary velocity see in Eq. (5) [13].

$$\underline{r}_{rad} = \frac{p - r_c}{|p - r_c|} \tag{3}$$

$$\underline{v}_{rad} = (\underline{v}_{sec} \cdot \underline{r}_{rad}) \cdot \underline{r}_{rad} \tag{4}$$

$$\underline{v}_{cir} = \underline{v}_{sec} - \underline{v}_{rad} \tag{5}$$

The slices were transformed in such way, that the slices are parallel with the global X-Y plane, with the Frenet normal matching to the X axis, and the origins of the local and global systems matching. This way the slices could be divided into an inner side (IS) (inner bend) and an outer side (OS) (outer bend). The various velocity components were averaged on these half slices. Python scripts were written to perform these calculations for every slice in all the timesteps. Thus, reducing the data, and enabling the examination of the results in both space and time.

3. RESULTS

In this section visualization techniques of the data will be explained, along with the findings, based on the comparisons of the cases with the control cases.

In order to represent the velocity fields in both space and time a 3D waterfall diagram would be needed which is hard to understand. Instead, a spatio-temporal contour plot was chosen, as it allows the representation of the velocity magnitudes in a 2D form. All 4 velocity components were plotted, with the inner and outer sides separately. Along with the velocity various centreline attributes were plotted as well. These include the Inscribed Sphere Radius (ISR), torsion κ and curvature τ. With these additional data the velocity plots can be examined together with the geometry. As an example, a rise in axial velocity results in a drop in ISR. On the vertical axes of the velocity plots is time, and on the X axis is the length along the centreline. On the velocity plots both the systolic maximum velocity point and diastolic velocity minimum point of the heart cycle can be seen as horizontal lines. The systolic maximum is at 0.15 s and the diastolic minimum is at 0.4 s. The area of the aneurysm ostium (the inlet of the sack) is marked on the plots with a yellow shading. For the control cases the shaded area marks the site of the bifurcation.

After examining all 8 cases, a difference emerged between the normal and control cases. In the following section this will be shown and explained on two characteristic examples. C0064 was chosen as the control case, and C0066 as the one with an aneurysm, both came from the Aneurysk database. As the difference occurs on the outer side between the radial and circumferential components only these are shown here.

The plots for C0064 can be seen on Fig. 4. Both secondary velocity components show elevated values only at the site of the bifurcation. Their values

are similar, and span a similar area in both space and time. Also, the bifurcation can be clearly seen on the ISR plot, as at the bifurcation it increases.

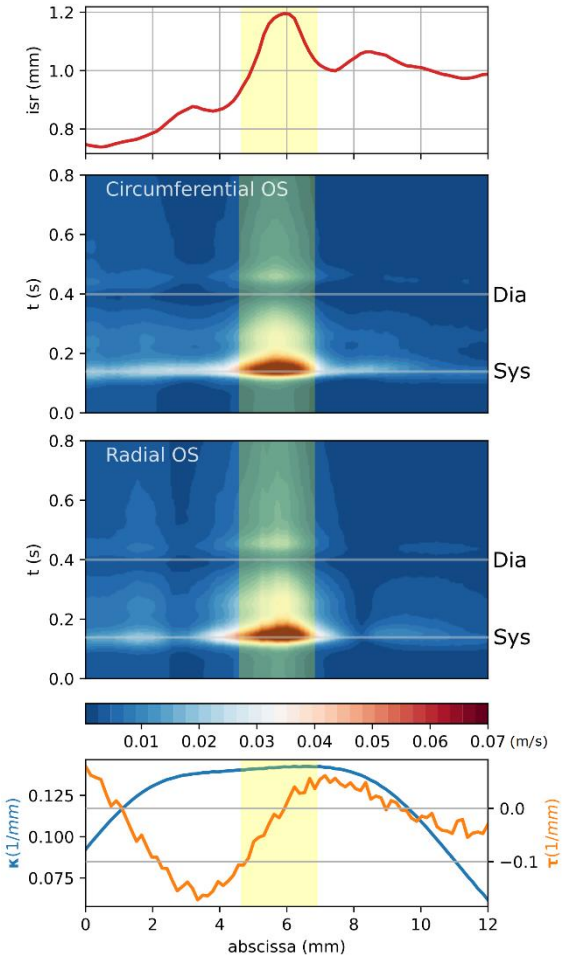

Figure 4. Plots for case C0064. Top: inscribed sphere radius along the centreline. Middle: spatio-temporal contour plots for the circumferential and radial velocity components. Bottom: curvature (blue line) and torsion (orange line) characteristics along the centreline. Yellow shading: bifurcation site

The plots for C0066 can be seen in Fig. 5. here we see a stark difference between the plots of the radial and circumferential components on the outer side. The radial velocity has an elevated zone at diastole at the site of the aneurysm, but its extent is small in both space and time, also the velocity values are not as high compared to the rest of the diagram. Looking at the circumferential diagram it is the opposite. The velocity component reaches higher values, and this elevated zone extends longer, covering a bigger area, and all of the area of the aneurysm opening. It also extends more in time, nearly till the diastolic point. Thus, creating a strong circumferential wash at the site of the aneurysm for a non-marginal part of a heart cycle. Similar plots were observed with the other reconstructed cases too.

Also, in this case the effect of the smaller artery after the bifurcation can be seen on the secondary component diagrams. The accelerating axial flow calms down the secondary components quicker than on the other side, where the diameter is larger.

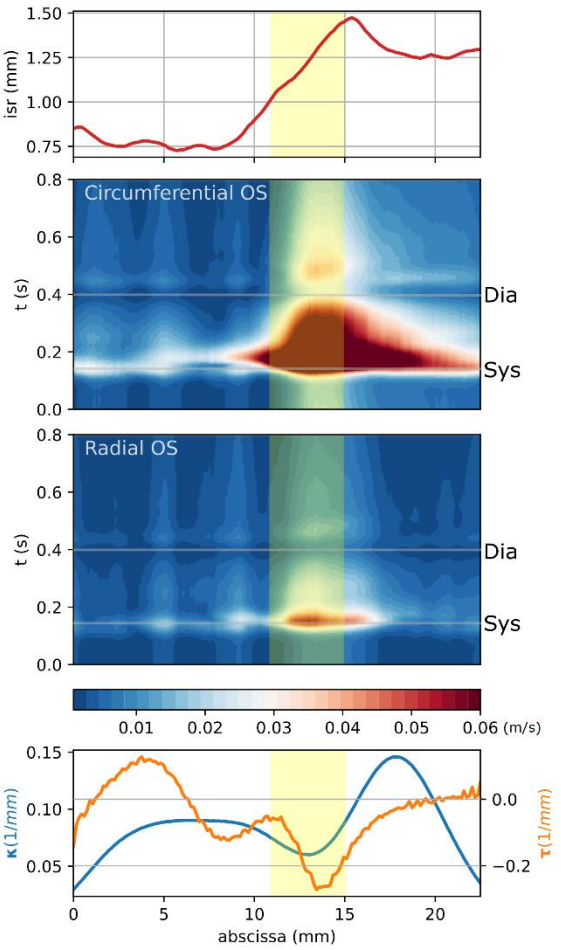

Figure 5. Plots for case C0066. Explanations are the same as in Figure 4. except for the yellow shading, here it marks the site of the aneurysm

4 CONCLUSIONS

This paper focused on the secondary flow characteristics at the site of bifurcation aneurysms. It is believed that elevated secondary flows play a key role in the formation of aneurysms, but it is a complicated biomechanical process, and it has not been fully understood yet.

Four geometries were reconstructed to their pre disease state using an objective interpolation-based method. Transient CFD simulations were run on these four cases along with four control cases. The secondary velocity field was decomposed into radial and circumferential components in a way to allow studying the results in both space and time.

After comparing the results, the secondary components differ on the outer side at the bifurcation between the control and reconstructed cases. On the control cases the radial and circumferential velocities

were comparable in strength. and the elevated velocity zone was comparable in space and time and was concentrated at the diastole time. In the case of the reconstructed geometries, the radial velocity strength was less than the circumferential component. Also, the elevated velocity zone of the circumferential component was more spread in space, but also time. This is in line with the hypothesis that the secondary flow of the blood plays a role in the formation of the aneurysm. Based on these eight cases there are definitive characteristic differences between the control and reconstructed cases, so more cases will be examined to confirm the findings of this paper.

ACKNOWLEDGEMENTS

The conference participation was supported by the Végh Gábor Neurointervention Fundation and by the Hungarian Brain Research Program under the Contract Number 2017-1.2.1-NAP2017-00002.

REFERENCES

[1] D. M. Sforza, C. M. Putman, and J. R. Cebral, "Hemodynamics of Cerebral Aneurysms," *Annual Review of Fluid Mechanics*, 2009, doi: 10.1146/annurev.fluid.40.111406.102126.

[2] B. Csippa, G. Závodszky, G. Paál, and I. Szikora, "A new hypothesis on the role of vessel topology in cerebral aneurysm initiation," *Computers in Biology and Medicine*, vol. 103, no. June, pp. 244–251, 2018, doi: 10.1016/j.compbiomed.2018.10.018.

[3] Á. Ugron and G. Paál, "On the boundary conditions of cerebral aneurysm simulations," *Periodica Polytechnica Mechanical Engineering*, vol. 58, no. 1, pp. 37–45, 2014, doi: 10.3311/PPme.7392.

[4] Aneurisk-Team, "{AneuriskWeb project website}, http://ecm2.mathcs.emory.edu/aneuriskweb." 2012. [Online]. Available: http://ecm2.mathcs.emory.edu/aneuriskweb

[5] A. W. Bergersen, H. A. Kjeldsberg, and K. Valen-Sendstad, "A framework for automated and objective modification of tubular structures: Application to the internal carotid artery," *International Journal for Numerical Methods in Biomedical Engineering*, vol. 36, no. 5, pp. 1–18, 2020, doi: 10.1002/cnm.3330.

[6] H. Kjeldsberg, A. Bergersen, and K. Valen-Sendstad, "morphMan: Automated manipulation of vascular geometries," *Journal of Open Source Software*, vol. 4, no. 35, p. 1065, 2019, doi: 10.21105/joss.01065.

[7] M. D. Ford, Y. Hoi, M. Piccinelli, L. Antiga, and D. A. Steinman, "An objective approach to digital removal of saccular aneurysms: Technique and applications," *British Journal of Radiology*, vol. 82, no. SPEC. ISSUE 1, pp. 55–61, 2009, doi: 10.1259/bjr/67593727.

[8] A. W. Bergersen, C. Chnafa, D. Gallo, M. Piccinelli, D. A. Steinman, and K. Valen-Sendstad, "Automated and objective removal of bifurcation aneurysms: Incremental improvements, and validation against healthy controls," *Journal of Biomechanics*, vol. 96, p. 109342, 2019, doi: 10.1016/j.jbiomech.2019.109342.

[9] J. R. Cebral, M. A. Castro, C. M. Putman, and N. Alperin, "Flow-area relationship in internal carotid and vertebral arteries," *Physiological Measurement*, vol. 29, no. 5, pp. 585–594, 2008, doi: 10.1088/0967-3334/29/5/005.

[10] H. G. Morales, I. Larrabide, A. J. Geers, M. L. Aguilar, and A. F. Frangi, "Newtonian and non-Newtonian blood flow in coiled cerebral aneurysms," *Journal of Biomechanics*, vol. 46, no. 13, pp. 2158–2164, 2013, doi: 10.1016/j.jbiomech.2013.06.034.

[11] C. Chnafa, O. Brina, V. M. Pereira, and D. A. Steinman, "Better Than Nothing: A Rational Approach for Minimizing the Impact of Outflow Strategy on Cerebrovascular Simulations," *American Journal of Neuroradiology*, vol. 39, no. 2, pp. 337–343, 2018, doi: 10.3174/ajnr.A5484.

[12] H. A. Kjeldsberg, A. W. Bergersen, and K. Valen-Sendstad, "Automated landmarking of bends in vascular structures: a comparative study with application to the internal carotid artery," *BioMedical Engineering Online*, vol. 20, no. 1, pp. 1–17, 2021, doi: 10.1186/s12938-021-00957-6.

[13] B. Csippa, L. Sándor, and G. Paál, "Decomposition of velocity field along a centerline curve using frenet-frames: Application to arterial blood flow simulations," *Periodica Polytechnica Mechanical Engineering*, vol. 65, no. 4, pp. 374–384, 2021, doi: 10.3311/PPME.18517.